Han *et al. J Mater Inf* 2023;3:24
DOI: 10.20517/jmi.2023.32

Journal of Materials Informatics

Research Article

Open Access

Regulating the electrocatalytic performance for nitrogen reduction reaction by tuning the N contents in $Fe_3@N_xC_{20-x}$ (x = 0~4): a DFT exploration

Bing Han, Fengyu Li*

School of Physical Science and Technology, Inner Mongolia University, Hohhot 010021, Inner Mongolia, China.

***Correspondence to:** Prof. Fengyu Li, School of Physical Science and Technology, Inner Mongolia University, No. 235 Daxue West Road, Saihan District, Hohhot 010021, Inner Mongolia, China. E-mail: fengyuli@imu.edu.cn

How to cite this article: Han B, Li F. Regulating the electrocatalytic performance for nitrogen reduction reaction by tuning the N contents in $Fe_3@N_xC_{20-x}$ (x = 0~4): a DFT exploration. *J Mater Inf* 2023;3:24. https://dx.doi.org/10.20517/jmi.2023.32

Received: 11 Sep 2023 **First Decision:** 28 Sep 2023 **Revised:** 20 Oct 2023 **Accepted:** 31 Oct 2023 **Published:** 3 Nov 2023

Academic Editors: Zhongfang Chen, Ming Hu **Copy Editor:** Pei-Yun Wang **Production Editor:** Pei-Yun Wang

Abstract

The Haber-Bosch (H-B) process, which is widely used in industry to synthesize ammonia, leads to serious energy and environment-related issues. The electrochemical nitrogen reduction reaction (eNRR) is the most promising candidate to replace H-B processes because it is more energy-efficient and environmentally friendly. Atomic-level catalysts, such as single-atom and double-atom catalysts (SACs and DACs), are of great interest due to their high atomic utilization and activity. The synergy between the metal atoms and two-dimensional (2D) support not only modulates the local electronic structure of the catalyst but also controls the catalytic performance. In this article, we explored the eNRR performance of 2D $Fe_3@N_xC_{20-x}$ (x = 0~4), whose structure was based on the experimentally synthesized $Ag_3@C_{20}$ sheet, by means of density functional theory calculations. Through calculations, we found that the 2D $Fe_3@N_4C_{16}$ with Fe_2 site coordinated with four N is a promising eNRR catalyst: the limiting potential is as low as -0.45 V, and the competing hydrogen evolution reaction can be effectively suppressed. Our work not only confirms that the coordination environment of the metal site is crucial for the electrocatalytic activity but also provides a new guideline for designing low-cost eNRR catalysts with high efficiency.

Keywords: Electrochemical nitrogen reduction reaction, two dimensions, single-atom and double-atom catalysts, active site, coordination, density functional theory

INTRODUCTION

Ammonia is a raw material vital to the global economy because of its wide range to be converted into fertilizers, chemicals, future fuel substitutes, and hydrogen storage[1]. The direct conversion of nitrogen in the air into ammonia is of paramount importance to both human beings and the planet's ecosystem[2]. Yet, the Haber-Bosch (H-B) process, the main traditional process for producing ammonia in industry, requires extremely demanding conditions, such as high temperatures and pressures[3-5]. Furthermore, the hydrogen in the H-B process is derived from natural gas or methane[6], which means that the process will release large amounts of CO_2[7]. Electrocatalytic nitrogen reduction reactions (eNRR) have been attracting increasing interest because of the mild reaction conditions compared to those of the H-B process; the reaction can be carried out under ambient conditions with the assistance of renewable electricity[8,9]. In addition, the source of hydrogen from water and the energy resource required for the eNRR process can be renewable, thus eliminating the negative impact of fossil fuels as the source of hydrogen and energy[1]. However, eNRR is a complex reaction involving six electron transfer processes, which is kinetically and thermodynamically more difficult compared to the hydrogen evolution reaction (HER), thus making the protons and electrons on the electrocatalyst susceptible to the production of H_2 rather than NH_3[10]. Therefore, it is desirable to develop catalysts for eNRR with high conversion and effective HER inhibition[11].

Many candidates could be used as eNRR electrocatalysts, for example Chen *et al.* used plasma-etched Ti_2O_3 (OV-Ti_2O_3) with oxygen vacancies to obtain maximum NH_3 yield up to 37.24 $\mu g \cdot h^{-1} \cdot mg_{cat.}^{-1}$ in 0.1 M HCl[12], and they proposed a mixture of titanium dioxide and effusus-derived carbon microtubes with three-dimensional cross-linked hollow tubular structures, which gave NH_3 yield as high as 20.03 $\mu g \cdot h^{-1} \cdot mg_{cat.}^{-1}$ in 0.1 M Na_2SO_4[13]. The single-atom catalysts (SACs)[14], which offer a new way to maximize the efficiency of metal atom use, have emerged as promising candidates[15]. The localized structures of the metal atoms allow them to exhibit excellent electronic properties and catalytic performance in a variety of chemical reactions[16]. However, the surface free energy of metals increases significantly with decreasing particle size, and metal atoms tend to aggregate[17]. Additionally, the stability of SACs in practical reactions depends on the surface configuration, the substrate, the reactants, and the limited temperature/pressure, which are not well defined and vary from one system to another[18]. The appropriate choice of substrates is a major (and in some cases a critical) factor in determining the catalytic performance of the catalyst, which should provide a large specific area to accommodate the metal sites and be able to modulate the local geometry and electronic structure of the metal atoms in the reaction, thus determining the overall catalytic performance[19]. Two-dimensional (2D) carbon[11,20], N-doped carbon[21-24], *etc.*[25-28], used as substrates for metal atoms as atomic catalysts, exhibit excellent efficiency toward eNRR. As an extension of SACs, double-atom catalysts (DACs) became another research hotspot due to their higher metal loading than SACs[22]. In terms of the overall reaction, DACs have multiple active sites (top and bridge) since their active centers are composed of two adjacent metal atoms, which can significantly improve the Faraday efficiency[29]. The bridge-site adsorption behavior of metal-metal atoms was found to exhibit a strong synergistic effect of modulating the electronic structure and promoting adsorption[30]. In addition, differences in surface states in different homonuclear or heteronuclear DACs can have an important impact on the selectivity and activity of the reactions[31]. Thus, both SACs and DACs may be excellent electrocatalysts if the right substrate is chosen.

Previous studies revealed that excellent electrocatalytic performance for the nitrogen reduction reaction (NRR) can be obtained by loading iron onto different substrates, whether as monoatoms[32-36], dimers[22,37-39], or other sizes[40-44]. In addition, given that the iron-molybdenum cofactor (FeMoco) is thought to be the site of dinitrogen reduction[45], we focused on Mo/Fe-containing catalysts. The chosen substrate was prompted by the recent experimental preparation of the 2D material Ag_3C_{20}[46], a planar structure with a rectangular lattice containing three Ag atoms and 20 C atoms. The three metal atoms in the lattice can be considered as

a single atom (M_1) and a bimetallic atom (M_2) site. In this work, we replaced the precious metal Ag atoms in $Ag_3@C_{20}$ with Mo/Fe atoms and obtained the $Mo_3/Fe_3@C_{20}$ monolayer. Through theoretical studies of the eNRR process, we found that $Mo_3@C_{20}$ is not suitable for eNRR due to its strong N_2 adsorption; in contrast, $Fe_3@C_{20}$ is a good eNRR catalyst (the limiting potential U_L = -0.59 V). With the demonstration that $Fe_3@C_{20}$ can be used as an electrocatalyst for eNRR, we substituted the C bonded with Fe by N to tune the coordination environment of the metal sites in order to further improve the catalytic efficiency. The limiting potential was further changed to -0.45 V when the N doping of the Fe_2 site was the maximum; i.e., all the four C bonded with Fe_2 sites were replaced by N with the stoichiometry of $Fe_3@N_4C_{16}$.

MATERIALS AND METHODS

All density functional theory (DFT) calculations were carried out using the Vienna *ab initio* Simulation Package (VASP)[47]. The Perdew, Burke, and Ernzerhof (PBE)[48] parameterization of the generalized gradient approximation (GGA) was used to describe the exchange-correlation function. The DFT-D2 dispersion correction scheme was applied for van der Waals (vdW) interactions[49]. A cut-off energy of 600 eV was used (convergence tests are shown in Supplementary Figure 1). The convergence parameters for force and energy were 0.02 eV/Å and 10^{-5} eV, respectively, and the convergence parameters were set the same as those in previous NRR calculations[50]. The Brillouin zone was sampled using a Monkhorst-Pack k-point grid[51] of 3 × 5 × 1. The Bader charge analysis[52] was employed to evaluate the charge transfer.

The adsorption energy of N_2 was calculated by $E_{ads} = E_{tot} - E_* - E_{N_2}$, where E_{tot}, E_*, and E_{N_2} are the total energy of N_2 adsorbed on the catalyst, the clean catalyst, and free N_2, respectively. The free energy G was obtained based on the computational hydrogen electrode (CHE) model proposed by Nørskov *et al.*[53], with the formula:

$$\Delta G = \Delta E + \Delta E_{ZPE} - T\Delta S + \Delta G_U + \Delta G_{pH}$$

In the above equation, E is the DFT energy, E_{ZPE} and S are the zero-point energy and entropy[54], respectively, E_{ZPE} and TS can be obtained by VASPKIT post-processing program[55], $\Delta G_U = -eU$, $\Delta G_{pH} = -k_B T \ln 10 \times pH$, k_B is the Boltzmann constant, T is 298.15 K[56], and the pH is zero in this study. The corrected values of the gas molecules and intermediates were given in Supplementary Tables 1 and 2, respectively. The limiting potential (U_L) of the entire reduction process was determined by the potential limiting step and was computed by $U_L = -\Delta G_{max}/e$[57].

We used the following equation for the formation energy of N doping:

$$E_f = E_{Fe_3@N_xC_{20-x}} - E_{Fe_3@C_{20}} - xE_N + xE_C$$

where $E_{Fe_3@N_xC_{20-x}}$ and $E_{Fe_3@C_{20}}$ are the energies of N-doped and pure $Fe_3@C_{20}$, respectively, x is the number of N atoms, and E_N and E_C represent the energies of a free N/C atom. All the details of the calculations and the results of the energy difference calculations are presented in Supplementary Table 3.

RESULTS AND DISCUSSION

The structure and the eNRR performance of the $M_3@C_{20}$ (M = Mo and Fe) monolayers

After structural optimization, the structures are represented by the $Fe_3@C_{20}$ shown in Figure 1A with rectangular lattice constants of a = 11.14 Å and b = 7.95 Å, and a = 11.59 Å and b = 8.45 Å for $Mo_3@C_{20}$,

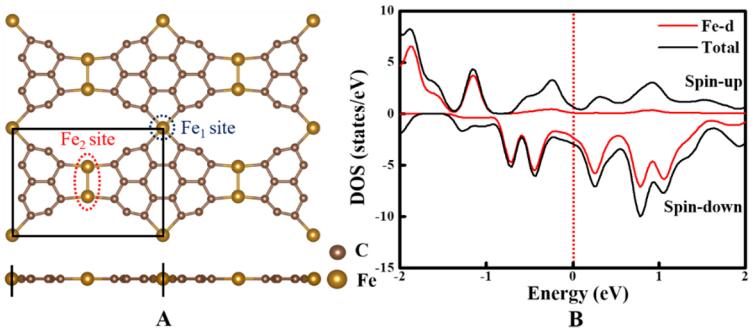

Figure 1. (A) Top and side views of the optimized 2D $Fe_3@C_{20}$ monolayer with the unit cell marked by black solid lines; (B) the partial density of states of the *d* orbitals of Fe atoms (red), and the DOS of the $Fe_3@C_{20}$ monolayer (black) with the Fermi level indicated by the red dashed line.

respectively. Due to the different loading positions of the metal atoms, they can be characterized as single-atom (M_1) and double-atom (M_2) sites (the Mo-Mo/Fe-Fe bond lengths at the diatomic sites are 2.85/2.22 Å, which also demonstrates the formation of metallic bonds in the M_2 sites). The results of the electron localization function (ELF: ELF values of 1.0 and 0.5, representing fully localized and free electron gases respectively, while ELF values close to 0 represent the low electron density region, Supplementary Figure 2) show that electron transfer from the Mo/Fe atoms to the C atoms, which is in line with the Bader charge analysis [Mo_1 (Mo_2): 1.16 (1.46) $|e|$ and Fe_1 (Fe_2): 0.96 (1.34) $|e|$]. The covalent bond between C and C atoms (1.32~1.47 Å) can also be identified. The total density of states (TDOS) [Figure 1B and Supplementary Figure 3] reveals that there are electronic states crossing the Fermi energy level, indicating the metallicity of both $Fe_3@C_{20}$ and $Mo_3@C_{20}$, which is beneficial to electrocatalysis.

For the electrochemical synthesis of ammonia, the adsorption of N_2 on the catalyst surface is the first step in the process. We considered two possible N_2 adsorption configurations, i.e., the side-on and end-on structures, on both M_1 and M_2 sites, respectively. The results are displayed in Figure 2 and Supplementary Figure 4. After N_2 adsorption onto $Mo_3@C_{20}$, the distances between N_2 and Mo after structural optimization ranged from 1.95 to 2.25 Å. It is noteworthy that when N_2 adsorbs to the Mo_2 site in the side-on conformation, it will spontaneously shift to the end-on conformation; thus, we only considered the end-on adsorption structure. The N–N bond lengths of N_2 at the Mo_1 (Mo_2) site in the side-on and end-on conformations are 1.21 and 1.14 (1.12) Å, respectively. The adsorption energies (E_{ads}) of N_2 at the Mo_1 (Mo_2) sites are all larger than 5.00 eV; such strong adsorption is not conducive to subsequent reactions or nitride releasing, and therefore $Mo_3@C_{20}$ is not suitable for the eNRR. In contrast, the distances between N of N_2 and Fe range from 1.88 to 3.13 Å. The N–N bond lengths of the adsorbed N_2 adopting side-on and end-on configurations are 1.11 (1.18) and 1.13 (1.14) Å at the Fe_1 (Fe_2) site, respectively, and the E_{ads} values of N_2 are -0.10 (-0.57) eV and -0.41 (-0.52) eV at the Fe_1 (Fe_2) site, respectively. In comparison with the 1.11 Å of N–N length of an isolated N_2 molecule, the N–N length is elongated, and the adsorbed N_2 is activated (also indicated by the considerable adsorption strength), except for the case of N_2 adsorbing on the Fe_1 site with side-on structures. The Bader charge analysis showed that the number of electrons transferred from Fe_1 (Fe_2) to the adsorbed N_2 with side-on and end-on configurations are 0.00 (0.49) and 0.16 (0.31) $|e|$, respectively, agreeing well with the adsorption strengths, which also suggests that the activation of N_2 at the Fe_2 site is more efficient than that at the Fe_1 site.

Before conducting the eNRR pathway test on the Fe_2 site, we evaluated the stability of $Fe_3@C_{20}$ by carrying out first-principles molecular dynamics (FPMD) simulations at 300 K for 5 ps (with a time step of 1 fs). The result showed that both the Fe_1 and Fe_2 moieties in the 2D structure were well preserved during the FPMD

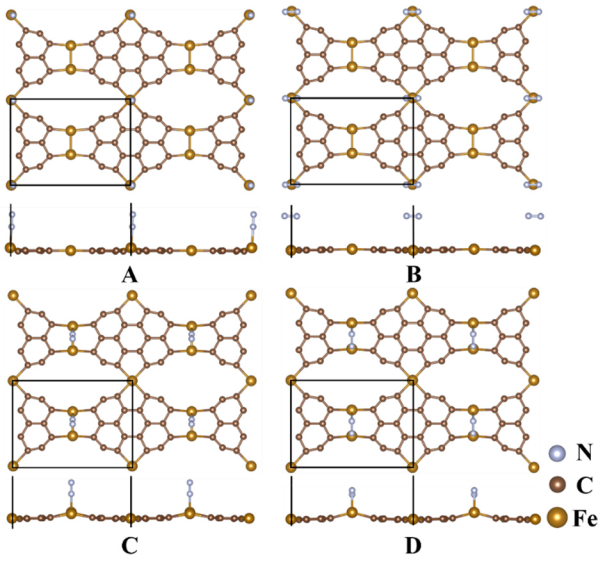

Figure 2. Different adsorption structures of N_2 on $Fe_3@C_{20}$: (A) end-on and (B) side-on configurations at Fe_1 sites; and (C) end-on and (D) side-on configurations at Fe_2 sites, with the unit cells marked by black lines.

simulations [Supplementary Figure 5], which demonstrates that $Fe_3@C_{20}$ has good thermodynamic stability.

The two eNRR pathways on the Fe_2 site of $Fe_3@C_{20}$ to produce ammonia started from side-on (end-on) adsorption are shown in Figure 3A and B, which are the enzymatic (alternative) mechanism [* → *N_2 → *NNH → *NHNH → *NH_2NH → *NH_2NH → *NH_2NH_2 → *NH_2 → *NH_3 → NH_3(g)] and the consecutive (distal) mechanism [*→ *N_2 → *NNH → *NNH_2 → *N → *NH_2 → *NH_3 → NH_3(g)], respectively. The main reasons for considering the above pathways can be assigned to the following two aspects: (1) N_2 has different adsorption configurations; (2) the proton-electron ($H^+ + e^-$) pairs attack N atoms in different manners [whether they attack one N atom consecutively first (consecutive/distal route) or attack the two N atoms alternatively (alternating/enzymatic path)].

Following the above mechanisms, the structural illustrations of each intermediate and free energy diagram are given in Figure 3. The results show that the change in free energy is preferred along the distal pathway. In detail, starting from the N_2 adsorbing with side-on configurations, the free energy change (ΔG) follows the sequence of -0.09, 0.64, 0.00, -0.12, -0.04, -1.82, 0.07, and 0.53 (-0.09, 0.64, 0.50, -1.05, -0.57, -0.87, 0.07, and 0.53) eV for each elementary step along the enzymatic (consecutive) route; while starting from the end-on adsorption of N_2, ΔG goes through -0.09, 0.59, -0.06, -0.20, 0.14, -1.83, 0.08, and 0.53 (-0.09, 0.59, -0.04, -0.47, -0.57, -0.87, 0.08, and 0.53) eV for each elementary step, along the alternative (distal) path. The potential determining step (PDS) is the first hydrogenation step of N_2 (*NN → *NNH) in the four eNRR pathways with the largest ΔG of 0.64 or 0.59 eV, which is comparable to that over Fe_3@gra (0.60 eV)[58] and smaller than that on Fe-C_2N (1.06 eV)[22]. The free energy change of releasing NH_3 [*NH_3 → NH_3(g), ΔG = 0.53 eV] is less than the ΔG of the first hydrogenating (ΔG = 0.64 or 0.59 eV), which is beneficial in facilitating the recovery of the catalyst.

The HER, requiring proton-electron pairs to proceed with the reaction, is the primary competitor against the eNRR. Therefore, we calculated the adsorption energy of *H and found E_{ads} of *H (-0.30 eV) > E_{ads} of *N_2 (-0.57/-0.52 eV) on the Fe_2 site. In addition, to exclude the possibility that the Fe_1 site may also proceed HER, lowering the selectivity towards eNRR, we also calculated E_{ads} of *H on the Fe_1 site (0.16 eV). All

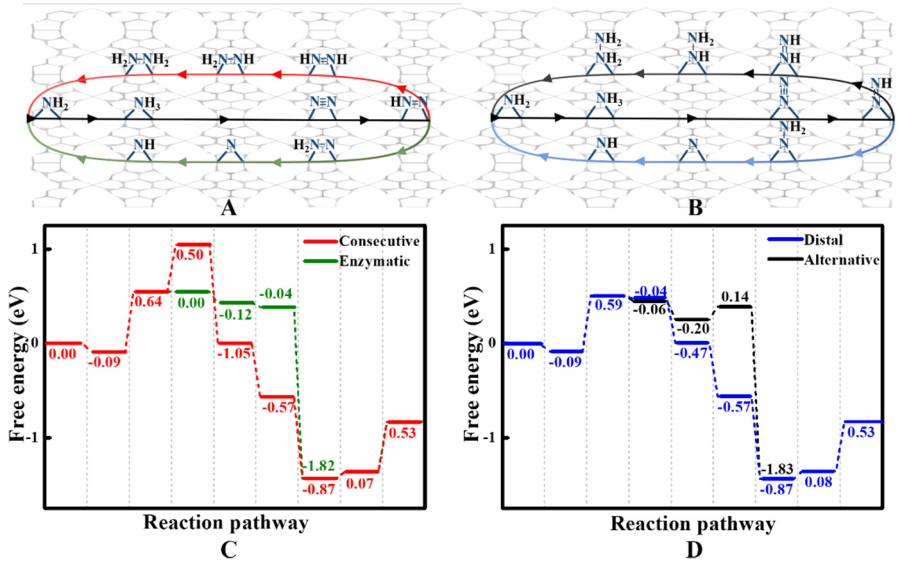

Figure 3. Different eNRR mechanisms on $Fe_3@C_{20}$ (A and B) and the free energy diagrams (C and D). Data denote the ΔG of each elementary step. eNRR: Electrochemical nitrogen reduction reaction.

results suggest that HER would be effectively suppressed over the $Fe_3@C_{20}$.

The geometry and the eNRR performance of the $Fe_3@N_xC_{20-x}$ (x = 1~4)

Previous studies showed that the catalytic performance of catalysts is associated with the coordination environment of the active site. Thus, 2D $Fe_3@N_xC_{20-x}$ ($x \leq 4$) materials were constructed by replacing Fe_2-bonded C with N, and all the optimized structures remain well with the initial plane [Supplementary Figure 6]. The formation energy of $Fe_3@N_xC_{20-x}$ decreases from -0.20 eV at x = 1 to -0.65 eV at x = 4 [Supplementary Table 3]. The lattice constants for these structures were given in Supplementary Table 4. Note that the N doping at x = 2 yields three structures, i.e., $Fe_3@N_2C_{18}$-I, $Fe_3@N_2C_{18}$-II and $Fe_3@N_2C_{18}$-III [Supplementary Figure 6B-D], with the lowest E_f (-0.50 eV) of asymmetric substitution $Fe_3@N_2C_{18}$-II compared to the other two structures (E_f = -0.22 eV for I and E_f = -0.35 eV for III). The lattice constant a/b decreases from 11.14/7.95 Å at x = 0 to 10.87/7.74 Å at x = 4, which can be understood by the smaller radius of N than that of C.

The adsorption energies of N_2 with side-on configurations on Fe_2 sites of most N-substituted monolayers are also stronger than those with end-on structures, and the adsorption strength decreases as the content of N increases, as demonstrated by the data in Supplementary Table 4: the E_{ads} values of the side/end-on adsorption configurations on Fe_2 sites of 2D $Fe_3@N_xC_{20-x}$ ($x \leq 4$) monolayers are -0.62/-0.55 eV for $Fe_3@N_1C_{19}$, -0.59/-0.55 eV for $Fe_3@N_2C_{18}$-I, -0.50/-0.48 eV for $Fe_3@N_2C_{18}$-II, -0.59/-0.52 eV for $Fe_3@N_2C_{18}$-III, -0.54/-0.52 eV for $Fe_3@N_3C_{17}$, and -0.20/-0.32 eV for $Fe_3@N_4C_{16}$, respectively. The N_2 adsorption structures are shown in Figure 4A and B, and Supplementary Figure 7. In the proceeding section, the PDSs for the considered routes on $Fe_3@C_{20}$ are the first hydrogenation step of N_2 ($*N_2 \rightarrow *NNH$). Then, we evaluate the ΔG values of the first hydrogenation step of N_2 on the Fe_2 site of 2D $Fe_3@N_xC_{20-x}$ ($x \leq 4$) [Supplementary Table 5]. The free energy changes on these N-substituted materials range from 0.45 to 1.23 eV. The ΔG values of the $Fe_3@N_1C_{19}$ (0.74 eV), $Fe_3@N_2C_{18}$-I (0.61 eV), $Fe_3@N_2C_{18}$-II (0.73 eV), $Fe_3@N_2C_{18}$-II (0.65 V), and $Fe_3@N_3C_{17}$ (0.67 V) are much smaller than those of the $FeCN_2$ (0.94 eV) and $FeCN_3$ (0.92 eV)[59], suggesting the more pronounced effect of the DAC environment than the SAC environment on the NRR performance. Unfortunately, all of them have free energy change values higher than 0.59 eV of $Fe_3@N_{20}$ [Figure 4C], and

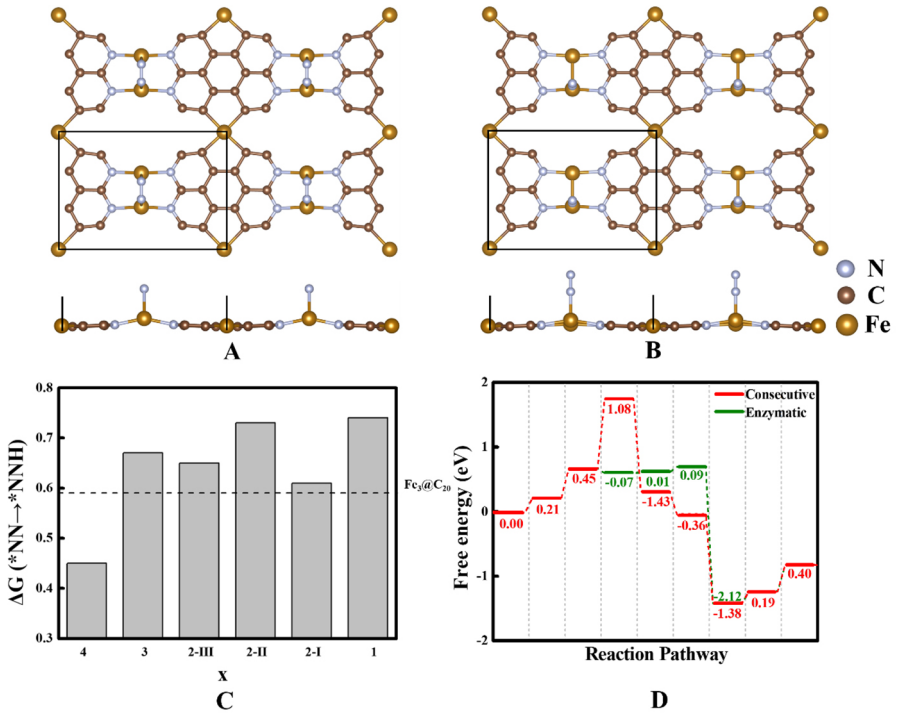

Figure 4. Top and side views of N_2 adsorbed at the Fe_2 site of $Fe_3@N_4C_{16}$ with the side-on configuration (A); the end-on configuration (B) with the unit cells marked by black lines; ΔG for the *NN → *NNH step of the energy preferred path for the $Fe_3@N_xC_{20-x}$ (x = 0-4) materials and the black dashed line indicates the free energy change value for $Fe_3@C_{20}$ (C) and the eNRR free energy diagram over the Fe_2 site of $Fe_3@N_4C_{16}$ (D). eNRR: Electrochemical nitrogen reduction reaction.

therefore, these subsequent pathways will not be considered. In contrast, the free energy change for the first hydrogenation of N_2 of side-on adsorption on $Fe_3@N_4C_{16}$ (0.45 eV) is smaller than that of $Fe_3@C_{20}$. It is worth noting that after the first hydrogenation of end-on adsorbed N_2, the *NNH configuration is automatically transformed to the side-on adsorbed *NNH configuration after structural optimization. Therefore, we only concentrated on the enzymatic and consecutive eNRR paths over $Fe_3@N_4C_{16}$.

On the $Fe_3@N_4C_{16}$, the free energy change for each elementary step along the enzymatic mechanism was 0.21, 0.45, -0.07, 0.01, 0.09, -2.12, 0.19, and 0.40 eV, and along the consecutive mechanism, it was 0.21, 0.45, 1.08, -1.43, -0.36, -1.38, 0.19 and 0.40 eV, respectively [Figure 4D]. Notably, although the ΔG of nitrogen adsorption is a positive value (0.21 eV), the adsorption energy before correction is negative (-0.20 eV), and the elongation of the N–N bond (1.17 Å) further suggests that the nitrogen was activated. However, in terms of the overall reaction, this small positive value is smaller than the free energy change in the first step of hydrogenation, i.e., *NN → *NNH (0.45 eV). As for the eNRR on the Fe_2 site of $Fe_3@N_4C_{16}$, the step *NN → *NNH becomes the PDS in the enzymatic mechanism, possessing a free energy change value of 0.45 eV, which is smaller than the values on $Fe_2Mo@C_6N_6$ (0.53 eV)[60] and Fe/Mo-N-C (0.63 eV)[61]. Furthermore, the free energy change of releasing the second NH_3(g) (0.40 eV) is also smaller than ΔG of the PDS (0.45 eV), indicating the feasibility of recovering the clean catalyst. In addition, we used the Poisson-Boltzmann implicit solvation model to simulate an aqueous solvent environment (with a dielectric constant of ε = 80)[62] to further explore the solvation effect on the eNRR performance of $Fe_3@N_4C_{16}$, and the results are shown in Supplementary Figure 8. The value of ΔG_{max} in the consecutive/enzymatic pathway on $Fe_3@N_4C_{16}$ with the solvent effect is reduced from 1.08/0.45 eV to 1.04/0.34 eV, which is consistent with the path selectivity of our calculations without solvent effect and demonstrates the selectivity of $Fe_3@N_4C_{16}$ to be

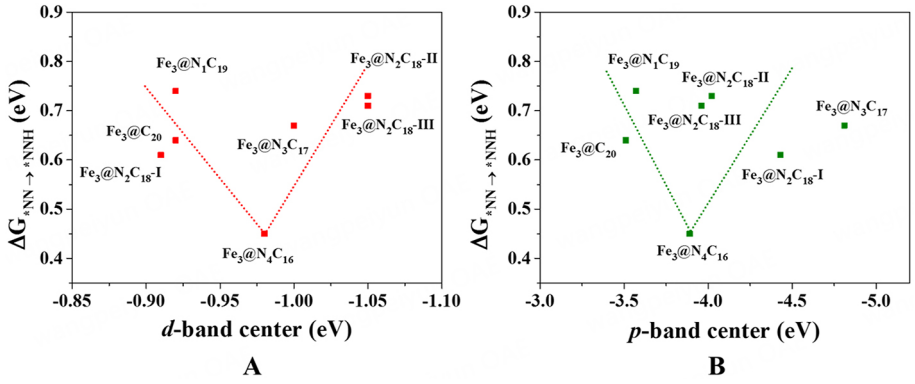

Figure 5. The variation of ΔG for the first hydrogenating of side-on N_2 against the *d*-band center (A) and *p*-band center of Fe_2-bonded C/N (B) for the $Fe_3@N_xC_{20-x}$ (x = 0-4).

an excellent NRR catalyst.

In addition, since the 2D $Fe_3@N_xC_{20-x}$ ($x \leq 4$) includes both Fe_1 and Fe_2 sites, to make sure that the Fe_2 site is the active site for eNRR to proceed, we also calculated the adsorption energy of N_2 at the Fe_1 site for comparison [Supplementary Table 4]. The adsorption energies of N_2 for the side-on/end-on adsorption configuration at the Fe_1 site are -0.11/-0.43 eV for $Fe_3@N_1C_{19}$, -0.06/-0.39 eV for $Fe_3@N_2C_{18}$-I, -0.08/-0.47 eV for $Fe_3@N_2C_{18}$-II, and -0.17/-0.43 eV for $Fe_3@N_2C_{18}$-III. For x = 1, 2, it indicates that N_2 prefers to adsorb at Fe_2 sites, while N_2 may prefer to adsorb on the Fe_1 site of $Fe_3@N_3C_{17}$ (-0.08/-0.58 eV) and $Fe_3@N_4C_{16}$ (0.15/-0.44 eV). Therefore, we further tested for further hydrogenation of N_2 (*NN → *NNH) on the Fe_1 site for x = 3, 4. However, the free energy changes for the first step of hydrogenation of N_2 end-on adsorbed on the Fe_1 site are 0.95 ($Fe_3@N_3C_{17}$) and 1.24 eV ($Fe_3@N_4C_{16}$), respectively. Such large free energy change is also unfavorable for eNRR, and for the reaction on $Fe_3@N_4C_{16}$, even though nitrogen tends to adopt end-on adsorption on the Fe_1 site, it is difficult to proceed the next step of the hydrogenation after this active site is occupied by nitrogen, and thus, the preferred N_2 adsorption on Fe_1 site will not affect the reaction on the Fe_2 site. Besides, to guarantee the selectivity towards eNRR instead of HER, the adsorption of *H at the Fe_1 site for x = 1~4. The adsorption strength of N_2 at Fe_2 sites prevails that of *H at Fe_2 (Fe_1) site: -0.62/-0.55 *vs.* -0.28 (0.24) eV for $Fe_3@N_1C_{19}$, -0.59/-0.55 *vs.* -0.48 (0.25) eV for $Fe_3@N_2C_{18}$-I, -0.50/-0.48 *vs.* -0.30 (0.65) eV for $Fe_3@N_2C_{18}$-II, -0.59/-0.52 *vs.* -0.24 (0.09) eV for $Fe_3@N_2C_{18}$-III, -0.59/-0.52 *vs.* -0.39 (0.23 eV) for $Fe_3@N_3C_{17}$, and -0.20/-0.32 *vs.* 0.02 (0.45) eV for $Fe_3@N_4C_{16}$.

All the above calculations show that the Fe_2 site remains the active center with N-doping varying from 1 to 4, and N-doping will not change the selectivity toward eNRR to HER. Most importantly, with the lowest ΔG_{max} and the preferent adsorption of N_2 against *H, $Fe_3@N_4C_{16}$ distinguishes itself as the most promising candidate for eNRR.

The origin of different eNRR performance of $Fe_3@N_xC_{20-x}$ (x = 0~4)

As an eNRR catalyst, the free energy change results show that the limiting potential of $Fe_3@N_4C_{16}$ (0.45 eV) is smaller than that of $Fe_3@C_{20}$ (0.59 eV) and is even better than the reported U_L values FeN_4/G (FeN_4 moiety embedded in graphene, 1.30 eV)[63] and FeN_4/FeMoPPc (FeN_4 moiety embedded with polyphthalocyanine, 0.66 eV)[64]. To figure out the origin of the significantly improved eNRR activity of $Fe_3@N_4C_{16}$, we analyzed the geometric and electronic structures of Fe_2 sites in $Fe_3@N_xC_{20-x}$ (x = 0~4). As illustrated in Supplementary Table 6, the Fe–Fe bond length of the Fe_2 site shows slight variation for x = 0~3 (d_{Fe-Fe} = 2.22~2.24 Å) and an obvious drop to 2.16 Å for x = 4, and the Fe_2-*d* orbitals exhibit a better hybridization with the adsorbed N_2-*p*

orbitals [Supplementary Figure 9], which further leads to more efficient activation of N–N as demonstrated by the lower ΔG of the first hydrogenating step. Besides, both the *d*-band center and the *p*-band center of Fe_2 -bonded C/N in $Fe_3@N_4C_{16}$ have moderate values among $Fe_3@N_xC_{20-x}$ (x = 0~4), showing an inverse volcano relationship [Figure 5 and Supplementary Table 6].

CONCLUSIONS

In summary, we theoretically investigated the eNRR performance of $Mo_3@C_{20}$ and $Fe_3@C_{20}$ monolayers based on the experimentally synthesized 2D $Ag_3@C_{20}$ structure. Our calculations revealed that $Fe_3@C_{20}$ exhibits good activity and selectivity for eNRR with a predicted limiting potential of -0.59 V. By further investigation of the synergy between the active Fe_2 site and its coordination, we found that the N-containing environment would tune the electronic properties and, thus, enhance the catalytic efficiency, where 2D $Fe_3@N_4C_{16}$ is demonstrated as the superior electrocatalyst with a limiting potential of -0.45 V. Moreover, the Fe_2 sites in our designed $Fe_3@N_xC_{20-x}$ materials have much smaller ΔG_{max} than those of Fe-based SACs such as FeN_4/G (1.30 eV)[63], $FeCN_2$ (0.94 eV) and $FeCN_3$ (0.92 eV)[59], and the best candidate $Fe_3@N_4C_{16}$ also has smaller ΔG_{max} than that of the Fe-based triple-atom catalyst $Fe_3@C_2N$ (0.57 eV)[65]. These findings provide new ideas for the development of new eNRR catalysts following experimental fabrication to theoretical prediction to experimental guidelines and highlight the important role of the metal-coordination environment.

DECLARATIONS

Authors' contributions

Performed the computations and drafted the manuscript: Han B
Provided guidance and revised the manuscript: Li F

Availability of data and materials

Supplementary materials are available from the Journal of Materials Informatics or from the authors.

Financial support and sponsorship

This work was supported by the National Natural Science Foundation of China (11964024), the "Grassland Talents" project of the Inner Mongolia autonomous region (12000-12102613), and the young science and technology talents cultivation project of Inner Mongolia University (21200-5223708). We thank the computational support from Beijing PARATERA.

Conflicts of interest

All authors declared that there are no conflicts of interest.

Ethical approval and consent to participate

Not applicable.

Consent for publication

Not applicable.

REFERENCES

1. Foster SL, Bakovic SIP, Duda RD, et al. Catalysts for nitrogen reduction to ammonia. *Nat Catal* 2018;1:490-500. DOI
2. Wang S, Ichihara F, Pang H, Chen H, Ye J. Nitrogen fixation reaction derived from nanostructured catalytic materials. *Adv Funct*

Mater 2018;28:1803309. DOI
3. Liu H. Ammonia synthesis catalyst 100 years: practice, enlightenment and challenge. *Chinese J Catal* 2014;35:1619-40. DOI
4. Guo X, Huang S. Tuning nitrogen reduction reaction activity via controllable Fe magnetic moment: a computational study of single Fe atom supported on defective graphene. *Electrochim Acta* 2018;284:392-9. DOI
5. Chen ZW, Lang XY, Jiang Q. Discovery of cobweb-like MoC_6 and its application for nitrogen fixation. *J Mater Chem A* 2018;6:9623-8. DOI
6. Ritter SK. Iron's star rising. *Chem Eng News* 2008;86:53-7. DOI
7. Bai J, Huang H, Li FM, et al. Glycerol oxidation assisted electrocatalytic nitrogen reduction: ammonia and glyceraldehyde co-production on bimetallic RhCu ultrathin nanoflake nanoaggregates. *J Mater Chem A* 2019;7:21149-56. DOI
8. Wang F, Mao J. Effect of N-doping on graphene: NRR activity and N-source. *Diam Relat Mater* 2021;118:108494. DOI
9. Choi C, Back S, Kim NY, Lim J, Kim YH, Jung Y. Suppression of hydrogen evolution reaction in electrochemical N_2 reduction using single-atom catalysts: a computational guideline. *ACS Catal* 2018;8:7517-25. DOI
10. Liu Q, Xu T, Luo Y, et al. Recent advances in strategies for highly selective electrocatalytic N_2 reduction toward ambient NH_3 synthesis. *Curr Opin Electrochem* 2021;29:100766. DOI
11. Li M, Cui Y, Zhang X, Luo Y, Dai Y, Huang Y. Screening a suitable Mo form supported on graphdiyne for effectively electrocatalytic N_2 reduction reaction: from atomic catalyst to cluster catalyst. *J Phys Chem Lett* 2020;11:8128-37. DOI PubMed
12. Chen H, Xu Z, Sun S, et al. Plasma-etched Ti_2O_3 with oxygen vacancies for enhanced NH_3 electrosynthesis and Zn-N_2 batteries. *Inorg Chem Front* 2022;9:4608-13. DOI
13. Chen H, Liang J, Dong K, et al. Ambient electrochemical N_2-to-NH_3 conversion catalyzed by TiO_2 decorated juncus effusus-derived carbon microtubes. *Inorg Chem Front* 2022;9:1514-9. DOI
14. Qiao B, Wang A, Yang X, et al. Single-atom catalysis of CO oxidation using Pt_1/FeO*x*. *Nat Chem* 2011;3:634-41. DOI
15. Zhang W, Fu Q, Luo Q, Sheng L, Yang J. Understanding single-atom catalysis in view of theory. *JACS Au* 2021;1:2130-45. DOI PubMed PMC
16. Wang Z, Yu Z, Zhao J. Computational screening of a single transition metal atom supported on the C_2N monolayer for electrochemical ammonia synthesis. *Phys Chem Chem Phys* 2018;20:12835-44. DOI
17. Chen Z, Zhao J, Cabrera CR, Chen Z. Computational screening of efficient single-atom catalysts based on graphitic carbon nitride (g-C_3N_4) for nitrogen electroreduction. *Small Methods* 2019;3:1800368. DOI
18. Liu JC, Tang Y, Wang YG, Zhang T, Li J. Theoretical understanding of the stability of single-atom catalysts. *Natl Sci Rev* 2018;5:638-41. DOI
19. Pan Y, Zhang C, Liu Z, Chen C, Li Y. Structural regulation with atomic-level precision: from single-atomic site to diatomic and atomic interface catalysis. *Matter* 2020;2:78-110. DOI
20. Zou H, Arachchige LJ, Rong W, et al. Low-valence metal single atoms on graphdiyne promotes electrochemical nitrogen reduction via M-to-N_2 π-backdonation. *Adv Funct Mater* 2022;32:2200333. DOI
21. Long J, Fu X, Xiao J. The rational design of single-atom catalysts for electrochemical ammonia synthesis *via* a descriptor-based approach. *J Mater Chem A* 2020;8:17078-88. DOI
22. Chen ZW, Yan JM, Jiang Q. Single or double: which is the altar of atomic catalysts for nitrogen reduction reaction? *Small Methods* 2019;3:1800291. DOI
23. Zhang X, Chen A, Zhang Z, Zhou Z. Double-atom catalysts: transition metal dimer-anchored C_2N monolayers as N_2 fixation electrocatalysts. *J Mater Chem A* 2018;6:18599-604. DOI
24. Wang YH, Dong JH, Tan Z, Wang XF, Song XZ. The journey of iron-based electrocatalytic materials for nitrogen reduction reaction: from current status to future prospects. *J Mater Chem A* 2023;11:11048-77. DOI
25. Sathishkumar N, Chen HT. Regulating the coordination environment of single-atom catalysts anchored on thiophene linked porphyrin for an efficient nitrogen reduction reaction. *ACS Appl Mater Interfaces* 2023;15:15545-60. DOI PubMed
26. Hou P, Huang Y, Ma F, et al. Screening of single-atom catalysts of transition metal supported on $MoSe_2$ for high-efficiency nitrogen reduction reaction. *Mol Catal* 2023;537:112967. DOI
27. Xu T, Liang J, Li S, et al. Recent advances in nonprecious metal oxide electrocatalysts and photocatalysts for N_2 reduction reaction under ambient condition. *Small Sci* 2021;1:2000069. DOI
28. Cheng H, Ding LX, Chen GF, Zhang L, Xue J, Wang H. Molybdenum carbide nanodots enable efficient electrocatalytic nitrogen fixation under ambient conditions. *Adv Mater* 2018;30:1803694. DOI
29. Li R, Wang D. Superiority of dual-atom catalysts in electrocatalysis: one step further than single-atom catalysts. *Adv Energy Mater* 2022;12:2103564. DOI
30. Yang W, Jia Z, Chen L, et al. Effects of intermetal distance on the electrochemistry-induced surface coverage of M-N-C dual-atom catalysts. *Chem Commun* 2023;59:10761-4. DOI
31. Yang W, Jia Z, Zhou B, et al. Why is C–C coupling in CO_2 reduction still difficult on dual-atom electrocatalysts? *ACS Catal* 2023;13:9695-705. DOI
32. Chen Z, Liu C, Sun L, Wang T. Progress of experimental and computational catalyst design for electrochemical nitrogen fixation. *ACS Catal* 2022;12:8936-75. DOI
33. Liu Y, Fan X, Bian W, et al. High-loading Fe_1 sites on vanadium disulfides: a scalable and non-defect-stabilized single atom catalyst for electrochemical nitrogen reduction. *J Mater Chem A* 2022;10:21142-8. DOI

34. Zhao X, Zhang X, Xue Z, Chen W, Zhou Z, Mu T. Fe nanodot-decorated MoS_2 nanosheets on carbon cloth: an efficient and flexible electrode for ambient ammonia synthesis. *J Mater Chem A* 2019;7:27417-22. DOI
35. Banerjee A. Computational screening of χ_3 borophene based single-atom catalysts for N_2 reduction. *Catal Today* 2023;418:114079. DOI
36. Sahoo SK, Heske J, Antonietti M, Qin Q, Oschatz M, Kühne TD. Electrochemical N_2 reduction to ammonia using single Au/Fe atoms supported on nitrogen-doped porous carbon. *ACS Appl Energy Mater* 2020;3:10061-9. DOI PubMed PMC
37. Zhang H, Cui C, Luo Z. MoS_2-supported Fe_2 clusters catalyzing nitrogen reduction reaction to produce ammonia. *J Phys Chem C* 2020;124:6260-6. DOI
38. Yao X, Zhang Z, Chen L, Chen ZW, Zhu YF, Singh CV. Work function-tailored nitrogenase-like Fe double-atom catalysts on transition metal dichalcogenides for nitrogen fixation. *ACS Sustainable Chem Eng* 2023;11:4990-7. DOI
39. Zhang Z, Huang X, Xu H. Anchoring an Fe dimer on nitrogen-doped graphene toward highly efficient electrocatalytic ammonia synthesis. *ACS Appl Mater Interfaces* 2021;13:43632-40. DOI PubMed
40. Liu JC, Ma XL, Li Y, Wang YG, Xiao H, Li J. Heterogeneous Fe_3 single-cluster catalyst for ammonia synthesis via an associative mechanism. *Nat Commun* 2018;9:1610. DOI PubMed PMC
41. Chen S, Gao Y, Wang W, Prezhdo OV, Xu L. Prediction of three-metal cluster catalysts on two-dimensional W_2N_3 support with integrated descriptors for electrocatalytic nitrogen reduction. *ACS Nano* 2023;17:1522-32. DOI
42. Xie K, Wang F, Wei F, Zhao J, Lin S. Revealing the origin of nitrogen electroreduction activity of molybdenum disulfide supported iron atoms. *J Phys Chem C* 2022;126:5180-8. DOI
43. Chen ZW, Chen LX, Jiang M, et al. A triple atom catalyst with ultrahigh loading potential for nitrogen electrochemical reduction. *J Mater Chem A* 2020;8:15086-93. DOI
44. Dai T, Lang X, Wang Z, Wen Z, Jiang Q. Rational design of an Fe cluster catalyst for robust nitrogen activation. *J Mater Chem A* 2021;9:21219-27. DOI
45. Lancaster KM, Roemelt M, Ettenhuber P, et al. X-ray emission spectroscopy evidences a central carbon in the nitrogenase iron-molybdenum cofactor. *Science* 2011;334:974-7. DOI PubMed PMC
46. Zhong Q, Niu K, Chen L, et al. Substrate-modulated synthesis of metal-organic hybrids by tunable multiple aryl-metal bonds. *J Am Chem Soc* 2022;144:8214-22. DOI
47. Kresse G, Furthmüller J. Efficient iterative schemes for *ab initio* total-energy calculations using a plane-wave basis set. *Phys Rev B Condens Matter* 1996;54:11169-86. DOI PubMed
48. Perdew JP, Burke K, Ernzerhof M. Generalized gradient approximation made simple. *Phys Rev Lett* 1996;77:3865-8. DOI PubMed
49. Bučko T, Hafner J, Lebègue S, Ángyán JG. Improved description of the structure of molecular and layered crystals: ab initio DFT calculations with van der Waals corrections. *J Phys Chem A* 2010;114:11814-24. DOI
50. Wang M, Huang Y, Ma F, et al. Theoretical insights into the mechanism of nitrogen-to-ammonia electroreduction on TM/g-C_9N_{10}. *Mol Catal* 2023;547:113391. DOI
51. Monkhorst HJ, Pack JD. Special points for Brillouin-zone integrations. *Phys Rev B* 1976;13:5188. DOI
52. Henkelman G, Arnaldsson A, Jónsson H. A fast and robust algorithm for Bader decomposition of charge density. *Comput Mater Sci* 2006;36:354-60. DOI
53. Nørskov JK, Rossmeisl J, Logadottir A, et al. Origin of the overpotential for oxygen reduction at a fuel-cell cathode. *J Phys Chem B* 2004;108:17886-92. DOI
54. Tian Y, Wang Y, Yan L, Zhao J, Su Z. Electrochemical reduction of carbon dioxide on the two-dimensional M_3(Hexaiminotriphenylene)$_2$ sheet: a computational study. *Appl Surf Sci* 2019;467-8:98-103. DOI
55. Wang V, Xu N, Liu JC, Tang G, Geng WT. VASPKIT: a user-friendly interface facilitating high-throughput computing and analysis using VASP code. *Comput Phys Commun* 2021;267:108033. DOI
56. Chen H, Handoko AD, Xiao J, et al. Catalytic effect on CO_2 electroreduction by hydroxyl-terminated two-dimensional MXenes. *ACS Appl Mater Interfaces* 2019;11:36571-9. DOI
57. Skúlason E, Bligaard T, Gudmundsdóttir S, et al. A theoretical evaluation of possible transition metal electro-catalysts for N_2 reduction. *Phys Chem Chem Phys* 2012;14:1235-45. DOI
58. Liu X, Li C, Ma P, Zhang W, Jia M, Song W. A first-principles study of transition metal clusters supported on graphene as electrocatalysts for N_2 to NH_3 reaction. *Mater Today Commun* 2023;35:106353. DOI
59. Guo Z, Liu C, Sun C, Xu J, Li H, Wang T. Tuning the coordination environment of single-atom iron catalysts towards effective nitrogen reduction. *ChemCatChem* 2023;15:e202300669. DOI
60. Wang S, Zhao T, Yan L. Tailoring of three-atom metal cluster catalysts for ammonia synthesis. *Catalysts* 2023;13:869. DOI
61. Gao S, Liu X, Wang Z, et al. Spin regulation for efficient electrocatalytic N_2 reduction over diatomic Fe-Mo catalyst. *J Colloid Interface Sci* 2023;630:215-23. DOI
62. Mathew K, Sundararaman R, Letchworth-Weaver K, Arias TA, Hennig RG. Implicit solvation model for density-functional study of nanocrystal surfaces and reaction pathways. *J Chem Phys* 2014;140:084106. DOI PubMed
63. Yuan D, Wu D, Zhang J, et al. Effect of oxygen coordination on the electrocatalytic nitrogen fixation of a vanadium single-atom catalyst embedded in graphene. *New J Chem* 2022;46:22936-43. DOI
64. Wang Y, Cheng W, Yuan P, et al. Boosting nitrogen reduction to ammonia on FeN_4 sites by atomic spin regulation. *Adv Sci* 2021;8:2102915. DOI PubMed PMC
65. Han B, Meng H, Li F, Zhao J. Fe_3 cluster anchored on the C_2N monolayer for efficient electrochemical nitrogen fixation. *Catalysts* 2020;10:974. DOI